

1 Word Count: 2849

2 **Revision 2**

3 **High-Pressure Phase Transition of Fe-bearing**
4 **Orthopyroxene Revealed by Raman Spectroscopy**

5 **LUO LI¹, XINYUE ZHANG¹, YINGXIN YU¹, ZHU MAO^{1,2,3*}**

6 ¹Deep Space Exploration Laboratory / School of Earth and Space Sciences, University of
7 Science and Technology of China, Hefei 230026, China

8 ²CAS Center for Excellence in Comparative Planetology, University of Science and Technology
9 of China, Hefei, Anhui 230026, China

10 ³Frontiers Science Center for Planetary Exploration and Emerging Technologies, University of
11 Science and Technology of China, Hefei, Anhui, 230026, China

12 *Corresponding authors: Zhu Mao (zhumao@ustc.edu.cn)

13

14

15

ABSTRACT

16
17 Orthopyroxene is one of the dominant minerals in the Earth's upper mantle. In this study, we
18 used Raman spectroscopy to investigate the lattice vibration and phase transition of
19 orthopyroxene with four different compositions using diamond anvil cells up to 34 GPa at 300 K.
20 Our orthopyroxene samples contain 0 (En₁₀₀), 9% (En₉₁Fs₉), 11% (En₈₆Fs₁₁) and 21% (En₇₄Fs₂₁)
21 Fe respectively. At ambient conditions, we observed that the Raman modes exhibited a negative
22 dependence on the Fe content, with the exception of the modes at ~850 and 930 cm⁻¹. In contrast,
23 the two Raman modes increase with increasing the Fe content. The phase transition from
24 metastable α - to β -phase was observed at 12.9-15 GPa for our orthopyroxene samples with less
25 than 21 mol.% Fe, and varying Fe content has a minor effect on the phase transition pressure.
26 Besides of Fe, additional 2-24 mol.% Al can cause phase transition pressure increase from 10-13
27 GPa to 14-16 GPa. At 29-30.1 GPa, we observed the second apparent change in the Raman
28 spectra for all of our investigated samples. For Fe-bearing orthopyroxene, this change in the
29 Raman spectra and frequency shift is associated with the phase transition from β - to γ -phase,
30 whereas for En₁₀₀, it should be caused by the change of coordination number Si from 4 to 6, or
31 the presence of α -popx phase. Using the obtained Raman frequency shifts, we have also
32 calculated the Grüneisen parameters at high pressures. These parameters are useful for
33 understanding the thermoelastic properties of orthopyroxene at high pressures.

34

35 **Keywords:** Raman spectroscopy, orthopyroxene, Fe content, phase transition, high pressure

36

37

38 1. INTRODUCTION

39 Orthopyroxene, $(\text{Mg}_{1-x}\text{Fe}_x)\text{SiO}_3$, is a crucial constituent of Earth's upper mantle (Bernard et al.,
40 2021; Herzberg and Gazel, 2009; Li et al., 2018; Shi et al., 2022; Tollan and Hermann, 2019).
41 According to the pyrolite model, the volume percentage of orthopyroxene is estimated to be 10
42 vol.% up to 350-km depth (Frost, 2008). Petrological observations suggest that the
43 orthopyroxene content in the subducted harzburgite and lherzolite layer can be as high as 22
44 vol.% (Bodinier and Godard, 2003; Ringwood, 1975; Ringwood and Irifune, 1988). Although
45 mantle orthopyroxene typically contains 6 mol.% Fe, some diamond inclusions originated from
46 100-500 km depth have shown that the Fe content in peridotitic orthopyroxene could vary from
47 3 and 19 mol.% (Stachel and Harris, 2008). In some high-pressure metamorphic rocks, the Fe
48 content in orthopyroxene exhibits a higher compositional range between 50 and 100 mol.%
49 (Brothers and Yokoyama, 1990; Davidson, 1968; Jaffe et al., 1978; White et al., 2001).
50 Therefore, investigating the physical properties of orthopyroxene with varying compositions
51 under relevant pressure and temperature conditions in the Earth's mantle is crucial for
52 understanding the structure and composition of the Earth's deep interior.

53

54 Along the normal mantle geotherm, the orthorhombic orthopyroxene (*Pbca* space group, α -
55 phase) transforms to high-pressure clinopyroxene (*C2/c* space group) at ~ 8 GPa and then
56 gradually dissolve into garnet at deeper depth (Akashi et al., 2009; Kung et al., 2005). However,
57 the path of phase transition in orthopyroxene at high pressures heavily relies on the temperature
58 and composition (Akashi et al., 2009). The transition of orthopyroxene to high-pressure
59 clinopyroxene will be inhibited when temperatures are significantly lower than the normal
60 mantle geotherm (Nishi et al., 2013; Van Mierlo et al., 2013). For example, the α - MgSiO_3

61 orthopyroxene (En_{100}) remains metastable and then transforms into its β -phase with a monoclinic
62 structure ($P2_1/c$ space group) at 10.5-13.3 GPa (Kung et al., 2004; Lin, 2004; Xu et al., 2018),
63 which can be preserved to ~ 40 GPa (Serghiou et al., 2000). Both α - and β -phase can remain
64 metastable up to 800 K at 520-km depth (Xu et al., 2020). Previous studies also investigated the
65 influence of Fe on the phase transition of orthopyroxene (Xu et al., 2020). For orthopyroxene
66 with 9 mol.% Fe ($\text{En}_{91}\text{Fs}_9$), the transition pressure from α - to β -phase is 12.3 GPa at 300 K,
67 which is similar to the Mg-endmember. However, Fe-bearing β -phase further transforms into the
68 γ -phase ($Pbca$ Space group) at 28.4 GPa (Finkelstein et al., 2015). Increasing the Fe content
69 from 30 to 82 mol.% only can weakly decrease the α - β phase transition pressure to 11 GPa and
70 lower the β - γ phase transition pressure to 12 GPa (Dera et al., 2013; Xu et al., 2020). But for
71 pure Fe endmember (Fs_{100}), orthopyroxene transforms into a different monoclinic β -phase with
72 space group $C2/c$ at ~ 6 GPa and then γ -phase at ~ 13 GPa (HughJones et al., 1996; Xu et al.,
73 2020). Experimental constraints on the transition from β - to γ -phase for orthopyroxene with less
74 than 20 mol.% Fe are still lacking.

75

76 Here, we have performed high-pressure Raman measurements to well constrain the phase
77 transition of orthopyroxene in four different compositions with varying Fe content in symmetric
78 diamond anvil cells (DACs) up to 34 GPa and 300 K. Results from Raman measurements can
79 also be used to identify orthopyroxenes as geological marker (Borromeo et al., 2022). The
80 collected Raman spectra were used to determine the influence of Fe content on the variation of
81 the vibration modes and help to identify the occurrence of the phase transition. Together with
82 previous thermal equation of state, we have calculated thermal Grüneisen parameters of

83 metastable phases at high pressures which are of great importance to calculate the thermal and
84 elastic properties of orthopyroxene.

85

86 **2. EXPERIMENTAL DETAILS**

87 Four orthopyroxene single-crystal samples were used in this study. Composition of these four
88 samples were analyzed using electron microprobe in the Key Laboratory of Crust-Mantle
89 Materials and Environments, University of Science and Technology of China (USTC). The
90 analysis yielded compositions of MgSiO_3 (En_{100}), $\text{Mg}_{0.91}\text{Fe}_{0.09}\text{SiO}_3$ ($\text{En}_{91}\text{Fs}_9$),
91 $\text{Mg}_{0.86}\text{Fe}_{0.11}\text{Al}_{0.02}\text{Ca}_{0.01}\text{Si}_{0.99}\text{O}_3$ ($\text{En}_{86}\text{Fs}_{11}$) and $\text{Mg}_{0.735}\text{Fe}_{0.21}\text{Al}_{0.07}\text{Si}_{0.965}\text{O}_3$ ($\text{En}_{74}\text{Fs}_{21}$). En_{100} ,
92 $\text{En}_{91}\text{Fs}_9$ and $\text{En}_{86}\text{Fs}_{11}$ are single crystals from Yangon, Myanmar. $\text{En}_{74}\text{Fs}_{21}$ was purchased from
93 Alfa Aesar Corp. Every sample was cut into random orientation with $\sim 25\ \mu\text{m}$ in diameter and
94 double-side polished to $\sim 25\ \mu\text{m}$ in thickness. Rhenium was used as gasket, and the gasket hole
95 was drilled to $235\ \mu\text{m}$ in diameter. Two ruby spheres were loaded into the sample chamber as the
96 pressure calibrant, and argon was used as the pressure medium for high pressure experiments
97 (Dewaele et al., 2004).

98

99 In-situ single-crystal Raman measurements were performed using symmetric DACs equipped
100 with a pair of $400\text{-}\mu\text{m}$ culet diamonds at the High-Pressure Mineral Physics Laboratory, USTC.
101 An Olympus flat field achromatic objective lens was employed for the collection of Raman
102 spectra with a 532-nm wavelength. The Raman spectra were measured in a backscattering
103 geometry in a confocal configuration. The Raman spectra at ambient conditions were determined
104 for all samples outside DACs. At high pressures, we have performed two runs of Raman

105 measurements on the intermediate composition including $\text{En}_{91}\text{Fs}_9$, $\text{En}_{86}\text{Fs}_{11}$ and $\text{En}_{74}\text{Fs}_{21}$. The
106 pure Mg-endmember orthopyroxene was carried out in one run.

107

108 **3. RESULTS**

109 At ambient conditions, 19 to 23 modes were observed for all the investigated orthopyroxene
110 samples. Typical Raman spectra of orthopyroxene with different Fe contents are shown in Figure
111 1. The frequencies of Raman-active modes for our four investigated samples at ambient
112 conditions are shown in Figure 2 and Tables 1-4. The measured frequencies for these
113 orthopyroxene samples are in good relevance with the Fe content. Most frequencies have shown
114 negative linear dependence on the Fe content. The Raman mode at $\sim 400\text{ cm}^{-1}$ for En_{100} shows a
115 similar linear decrease with Fe content up to 50 mol.% but exhibits a much stronger reduction by
116 further increasing the Fe content to 100 mol.%. In addition, we noted that there were two Raman
117 modes around $\sim 900\text{ cm}^{-1}$ increase with Fe content.

118

119 Based on the ambient conditions results, high-pressure Raman spectra for four samples were
120 collected up to 34 GPa at 300 K. For En_{100} , all the frequencies followed a nearly linear increase
121 with pressure up to 13.5 GPa. In exceed of 13.5 GPa, we observed the disappearance of modes at
122 ~ 425 , ~ 560 and $\sim 590\text{ cm}^{-1}$ accompanied with new modes at ~ 400 , ~ 500 and $\sim 855\text{ cm}^{-1}$. Similar
123 change in the Raman spectra and mode frequencies occur at 12.9 GPa for $\text{En}_{91}\text{Fs}_9$, 15 GPa for
124 $\text{En}_{86}\text{Fs}_{11}$ and $\text{En}_{74}\text{Fs}_{21}$ (Figures 4-6). Another obvious change in Raman spectra was noted to
125 occur at approximately 30 GPa for all the investigated orthopyroxene, characterized by the
126 variation in the pressure dependence of Raman frequencies.

127

128 **4. DISCUSSION**

129 **4.1. Raman modes at ambient conditions**

130 The obtained results were first used to understand the influence of Fe on the Raman frequency of
131 orthopyroxene at ambient conditions. Our Raman spectra of orthopyroxene are similar to
132 previous studies (Chopelas, 1999; Huang et al., 2000). Meaning of each Raman mode for
133 orthopyroxene has been well interpreted by Stangarone et al. (2016). The variation of the Raman
134 modes with Fe content are relevant to the vibrational frequency, ν , of a simple harmonic
135 oscillator (Huang et al., 2000; Stangarone et al., 2016), which can be expressed as:

$$\nu = \frac{1}{2\pi} \sqrt{\frac{k}{\mu}} \quad (1)$$

136 where μ is the reduced mass, k is the force constant which is assumed to be an inverse function
137 of interatomic distance. Addition of Fe increases the reduced mass, μ , and bond length of
138 orthopyroxene which explains the negative correlation of most Raman modes with Fe
139 substitution. When the Fe content in orthopyroxene is less than 50 mol.%, the Raman mode at
140 $\sim 400 \text{ cm}^{-1}$ exhibits a similar trend with pressure to most other modes. Yet further elevating the
141 Fe content above 50 mol.% in orthopyroxene produces an enhanced reduction in the mode
142 frequencies. This may be due to different substitution mechanism in orthopyroxene by varying
143 the Fe content. Fe primarily occupies the M2 sites when the Fe content in orthopyroxene is less
144 than 50 mol.%, whereas it starts to substitute Mg in the M1 sites when the abundance is greater
145 than 50% (Domeneghetti et al., 1995; Domeneghetti et al., 1985; Proyer et al., 2004; Stangarone
146 et al., 2016; Stangarone et al., 2023). The correlation of Raman frequency with Fe content is thus
147 mainly related to the variation of atomic mass, volume and bond length caused by Fe substitutes
148 for Mg.

149

150 **4.2. Phase transition of orthopyroxene**

151 We have also plotted the wavenumber of β - and γ -phase as function of Fe content at 16 and 30
152 GPa, respectively (Figures S1-S2 in the supplemental material). The Raman shifts of the β - and
153 γ -phase generally exhibit a negative correlation with Fe substitution, similar to the α -phase.
154 Specifically, around $\sim 1000\text{ cm}^{-1}$, the Raman mode for the β -phase increases with Fe content. The
155 phase transition in orthopyroxene at 300 K was determined by the frequency discontinuities and
156 change in the pressure dependence of some modes at high pressures (Figures 3-6). We identify
157 the α - to β -phase transition to occur at 13.5 GPa for En_{100} , 12.9 GPa for $\text{En}_{91}\text{Fs}_9$, 15 GPa for
158 $\text{En}_{86}\text{Fs}_{11}$, and 15 GPa for $\text{En}_{74}\text{Fs}_{21}$ (Figure 7). Together with previous experimental results, our
159 experimental results have shown that the α - β phase transition pressure for Al-free orthopyroxene
160 with varying Fe content is lower than the corresponding Al-bearing phase. Transition from the α -
161 to β -phase for Al-free orthopyroxene with less than 60 mol.% Fe occurs between 10 and 13 GPa
162 (Dera et al., 2013; Finkelstein et al., 2015; Lin, 2004; Xu et al., 2020; Xu et al., 2018; Zhang et
163 al., 2013a; Zhang et al., 2013b). Further elevating the Fe content above 60% leads to a dramatic
164 decrease in the phase transition pressure (Dera et al., 2013; Xu et al., 2020). Addition of Al leads
165 to an increase in the α - to β -phase transition pressure. Orthopyroxene with 2-24 mol.% Al has a
166 phase transition to occur at 14-16 GPa (Xu et al., 2022; Zhang et al., 2013b). In contrast, $\text{En}_{91}\text{Fs}_9$
167 contained virtually no other trace elements, consistent with previous research results. The phase
168 boundary of the En_{100} sample was found to be higher than those reported in previous studies,
169 primarily due to the large pressure intervals used in earlier experiments (Lin, 2004; Xu et al.,
170 2020; Xu et al., 2018; Zhang et al., 2013b).

171

172 The change in the pressure dependence of Raman modes at ~29 GPa for all of our orthopyroxene
173 samples except En₁₀₀ is related to the β- to γ-phase transition (Figure 7). We observed that in
174 En₁₀₀, the Raman frequencies at around ~650 and ~1100 cm⁻¹ have merged into a single mode,
175 each comprising three peaks. All the Raman modes above 31 GPa exhibit different pressure
176 dependence compared to modes between 14 and 30 GPa. This change in the Raman modes could
177 be related to the coordination number change of Si from 4 to 6 or the transition to α-popx phase
178 which have been reported by two previous experimental studies (Finkelstein et al., 2015;
179 Serghiou et al., 2000). Our experimental results indicate that the transition pressure from β- to γ-
180 phase are nearly independent of Fe when the Fe content in orthopyroxene is less than 60 mol.%.
181 Further increasing Fe content up to 82 mol.% leads to a substantial decrease in the phase
182 transition pressure (Dera et al., 2013; Xu et al., 2020). Once the Fe content in orthopyroxene is
183 above 80 mol.%, addition of Fe has minimum effect on the phase transition pressure to the γ-
184 phase. As a result, β-phase exists in a much narrow pressure range for orthopyroxene with 82-
185 100 mol.% than the corresponding phase with less than 82 mol.% Fe.

186

187 **4.3. Grüneisen parameters**

188 The obtained Raman frequency shifts allow us to derive the isothermal Grüneisen parameters at
189 high pressures. The isothermal Grüneisen parameter can be calculated as follows:

$$\gamma_i = -\frac{\partial \ln \nu_i}{\partial \ln V} = -\frac{V}{\nu_i} \frac{d\nu_i}{dV} = \frac{K_T}{\nu_i} \frac{d\nu_i}{dP} \quad (2)$$

190 where ν_i is the i^{th} mode of the lattice vibration, V is the unit-cell volume, and K_T is the isothermal
191 bulk modulus at a given pressure. The values of ν and $d\nu/dP$ were derived by fitting the
192 experimental data using a polynomial function in this study. The influence of Fe on the bulk
193 modulus of α-orthopyroxene at ambient conditions, K_{T0} , was summarized in Figure 8 using

194 previous experimental results (Dera et al., 2013; Hovis et al., 2021; Hugh-Jones and Angel, 1997;
195 Jackson et al., 2003; Nestola et al., 2008; Xu et al., 2020; Xu et al., 2022; Xu et al., 2018; Zhang
196 et al., 2013a; Zhao et al., 1995). There is a strong trade-off between the bulk modulus K_{T0} and its
197 pressure derivative, K' determined from the X ray diffraction study. For α -orthopyroxene, the
198 value of K' is greater than general mantle minerals with values ranging between 7.5 and 8.5.
199 Here, we used an average K' of 8 and re-analyzed previous experimental results to constrain K_{T0}
200 and obtained (Figure 8):

$$201 \quad K_{T0}(\alpha\text{-phase}) = -0.05X_{\text{Fe}} + 109.80$$

202 Experimental constraints on the equation of state and elastic properties of both β - and γ -phase are
203 limited (Xu et al., 2020; Xu et al., 2022; Xu et al., 2018). We used fixed $K'=4$ to derive K_{T0} , and
204 the effect of Fe on K_{T0} is (Figure 8):

$$205 \quad K_{T0}(\beta\text{-phase}) = 0.81X_{\text{Fe}} + 139.71$$

$$206 \quad K_{T0}(\gamma\text{-phase}) = -0.01X_{\text{Fe}} + 131.71$$

207 Grüneisen parameters, γ , at high pressures for each Raman mode was calculated and shown in
208 Table S5 in the supplemental material. In general, there is not a very clear correlation between
209 changes in Fe content and the γ value (Figure 9). In the α -phase, an increase in Fe content to 11%
210 leads to a decrease in γ for mode ν_{10} . Among the compositions, $\text{En}_{91}\text{Fs}_9$ exhibits a lower γ value
211 than the other three in the β -phase. In the γ -phase, there is no discernible trend in the γ value with
212 varying Fe content. For mode ν_{24} and ν_{32} in the α -phase, variations in Fe content have a
213 negligible influence on γ , considering calculation uncertainties. However, in both the β and γ -
214 phases, the relationship between changes in Fe content and the Grüneisen parameter remains
215 unclear.

216

217 **IMPLICATIONS**

218 Orthopyroxene is an important mineral component of the mantle, but the β - and γ -phases of
219 metastable orthopyroxene that exist above 10 GPa can only be present in the cold subduction
220 zone harzburgite and lherzolite layers with temperatures 700-1000 K lower than the normal
221 mantle (Finkelstein et al., 2015; Ganguly et al., 2009). The significance of our study lies in the
222 detailed characterization of the effect of Fe content changes on the structural phase transition of
223 metastable orthopyroxene and the influence of the transitions on the Grüneisen parameter, which
224 can be directly applied to understand the effects of compositional changes on the sound velocity
225 and density structure of cold harzburgite and lherzolite layers in the subduction slab. Combined
226 with previous high-pressure research results, we observed that the effect of Fe content changes
227 from 0-80% on the α - to β -phase transition pressure of orthopyroxene is small, and the transition
228 mainly occurs from the bottom of the upper mantle to the top of the transition zone. For instance,
229 the α - to β -phase transition for orthopyroxene with 11% Fe has a small effect on the longitudinal
230 and transverse wave velocities, less than 2%, and a density change of about 2% (Li et al., 2022).
231 Additionally, the transition from metastable β -orthopyroxene to γ -phase occurs at pressures
232 exceeding 29 GPa. Therefore, the possibility of metastable γ -phase for orthopyroxene with less
233 than 20% Fe existing in the mantle is small from the 300-K experimental results. However, the
234 Clapeyron slope of the β - γ phase boundary remains unknown. Further high pressures and
235 temperatures experimental research is thus needed which is crucial for our understanding of the
236 density and sound velocity structure of subduction slabs in response to compositional changes.

237

238

239

240

241

FUNDING

242 Z. Mao acknowledges supports from China National Science Foundation (42241117 and
243 42272036), the B-type Strategic Priority Program of the Chinese Academy of Sciences (Grant
244 No. XDB41000000), and the Fundamental Research Funds for the Central Universities
245 (WK2080000144).

246

247

REFERENCES CITED

- 248 Akashi, A., Nishihara, Y., Takahashi, E., Nakajima, Y., Tange, Y., and Funakoshi, K.-i. (2009)
249 Orthoenstatite/clinoenstatite phase transformation in MgSiO_3 at high-pressure and high-
250 temperature determined by in situ X-ray diffraction: Implications for nature of the X
251 discontinuity. *Journal of Geophysical Research-Solid Earth*, 114.
252 <https://doi.org/10.1029/2008jb005894>
- 253 Bernard, R.E., Schulte-Pelkum, V., and Behr, W.M. (2021) The competing effects of olivine and
254 orthopyroxene CPO on seismic anisotropy. *Tectonophysics*, 814, 228954.
- 255 Bodinier, J.-L., and Godard, M. (2003) Orogenic, Ophiolitic, and Abyssal Peridotites. *Treatise on*
256 *Geochemistry*, 2, 568. <https://doi.org/10.1016/b0-08-043751-6/02004-1>
- 257 Borromeo, L., Andò, S., Bersani, D., Garzanti, E., Gentile, P., Mantovani, L., and Tribaudino, M. (2022)
258 Detrital orthopyroxene as a tracer of geodynamic setting: A Raman and SEM-EDS provenance
259 study. *Chemical Geology*, 596, 120809.
260 <https://doi.org/https://doi.org/10.1016/j.chemgeo.2022.120809>
- 261 Brothers, R.N., and Yokoyama, K. (1990) Fe-rich pyroxenes from a microdiorite dike, Whangarei, New
262 Zealand. *American Mineralogist*, 75(5-6), 620-630.
- 263 Chopelas, A. (1999) Estimates of mantle relevant Clapeyron slopes in the MgSiO_3 system from high-
264 pressure spectroscopic data. *American Mineralogist*, 84(3), 233-244.
- 265 Davidson, L. (1968) Variation in ferrous iron-magnesium distribution coefficients of metamorphic
266 pyroxenes from Quairading, Western Australia. *Contributions to Mineralogy and Petrology*,
267 19(3), 239-259.
- 268 Dera, P., Finkelstein, G.J., Duffy, T.S., Downs, R.T., Meng, Y., Prakapenka, V., and Tkachev, S. (2013)
269 Metastable high-pressure transformations of orthoferrosilite Fs_{82} . *Physics of the Earth and*
270 *Planetary Interiors*, 221, 15-21. <https://doi.org/10.1016/j.pepi.2013.06.006>
- 271 Dewaele, A., Loubeyre, P., and Mezouar, M. (2004) Equations of state of six metals above 94 GPa.
272 *Physical Review B*, 70(9), 094112. <https://doi.org/https://doi.org/10.1103/physrevb.70.094112>
- 273 Domeneghetti, M.C., Molin, G.M., Stimpfl, M., and Tribaudino, M. (1995) Orthopyroxene from the Serra
274 de Magé Meteorite: Structure refinement and estimation of C2/c pyroxene contributions to
275 apparent Pbca diffraction violations. *American Mineralogist*, 80(9-10), 923-929.
- 276 Domeneghetti, M.C., Molin, G.M., and Tazzoli, V. (1985) Crystal-chemical implications of the Mg^{2+} - Fe^{2+}
277 distribution in orthopyroxenes. *American Mineralogist*, 70(9-10), 987-995.

- 278 Finkelstein, G.J., Dera, P.K., and Duffy, T.S. (2015) Phase transitions in orthopyroxene (En_{90}) to 49 GPa
279 from single-crystal X-ray diffraction. *Physics of the Earth and Planetary Interiors*, 244, 78-86.
280 <https://doi.org/https://doi.org/10.1016/j.pepi.2014.10.009>
- 281 Frost, D.J. (2008) The Upper Mantle and Transition Zone. *Elements*, 4(3), 171-176.
282 <https://doi.org/10.2113/gselements.4.3.171>
- 283 Ganguly, J., Freed, A.M., and Saxena, S.K. (2009) Density profiles of oceanic slabs and surrounding
284 mantle: Integrated thermodynamic and thermal modeling, and implications for the fate of slabs
285 at the 660 km discontinuity. *Physics of the Earth and Planetary Interiors*, 172(3), 257-267.
286 <https://doi.org/https://doi.org/10.1016/j.pepi.2008.10.005>
- 287 Herzberg, C., and Gazel, E. (2009) Petrological evidence for secular cooling in mantle plumes. *Nature*,
288 458(7238), 619-622.
- 289 Hovis, G.L., Tribaudino, M., Leaman, A., Almer, C., Altomare, C., Morris, M., Maksymiw, N., Morris, D.,
290 Jackson, K., and Scott, B. (2021) Thermal expansion of minerals in the pyroxene system and
291 examination of various thermal expansion models. *American Mineralogist: Journal of Earth and
292 Planetary Materials*, 106(6), 883-899.
- 293 Huang, E., Chen, C., Huang, T., Lin, E., and Xu, J.-a. (2000) Raman spectroscopic characteristics of Mg-Fe-
294 Ca pyroxenes. *American Mineralogist*, 85(3-4), 473-479.
- 295 Hugh-Jones, D., and Angel, R. (1997) Effect of Ca^{2+} and Fe^{2+} on the equation of state of MgSiO_3
296 orthopyroxene. *Journal of Geophysical Research: Solid Earth*, 102(B6), 12333-12340.
- 297 Hugh-Jones, D., Sharp, T., Angel, R., and Woodland, A. (1996) The transition of orthoferrosilite to high-
298 pressure $C2/c$ clinoferrosilite at ambient temperature. *European Journal of Mineralogy*, 8(6),
299 1337-1345.
- 300 Jackson, J.M., Palko, J.W., Andrault, D., Sinogeikin, S.V., Lakshtanov, D.L., Wang, J.Y., Bass, J.D., and Zha,
301 C.S. (2003) Thermal expansion of natural orthoenstatite to 1473 K. *European Journal of
302 Mineralogy*, 15(3), 469-473. <https://doi.org/10.1127/0935-1221/2003/0015-0469>
- 303 Jaffe, H., Robinson, P., and Tracy, R. (1978) Orthoferrosilite and other iron-rich pyroxenes in
304 micropertthite gneiss of the Mount Marcy area, Adirondack Mountains. *American Mineralogist*,
305 63(11-12), 1116-1136.
- 306 Kung, J., and Li, B. (2014) Lattice Dynamic Behavior of Orthoferrosilite (FeSiO_3) toward Phase Transition
307 under Compression. *The Journal of Physical Chemistry C*, 118(23), 12410-12419.
308 <https://doi.org/10.1021/jp4112926>
- 309 Kung, J., Li, B., Uchida, T., and Wang, Y. (2005) In-situ elasticity measurement for the unquenchable high-
310 pressure clinopyroxene phase: Implication for the upper mantle. *Geophysical Research Letters*,
311 32(1). <https://doi.org/https://doi.org/10.1029/2004GL021661>
- 312 Kung, J., Li, B.S., Uchida, T., Wang, Y.B., Neuville, D., and Liebermann, R.C. (2004) In situ measurements
313 of sound velocities and densities across the orthopyroxene \rightarrow high-pressure clinopyroxene
314 transition in MgSiO_3 at high pressure. *Physics of the Earth and Planetary Interiors*, 147(1), 27-44.
315 <https://doi.org/10.1016/j.pepi.2004.05.008>
- 316 Li, L., Sun, N., Shi, W., Mao, Z., Yu, Y., Zhang, Y., and Lin, J.F. (2022) Elastic Anomalies across the α - β
317 Phase Transition in Orthopyroxene: Implication for the Metastable Wedge in the Cold
318 Subduction Slab. *Geophysical Research Letters*, e2022GL099366.
- 319 Li, X., Zhang, L., Wei, C., Slabunov, A.I., and Bader, T. (2018) Quartz and orthopyroxene exsolution
320 lamellae in clinopyroxene and the metamorphic P-T path of Belomorian eclogites. *Journal of
321 Metamorphic Geology*, 36(1), 1-22.
- 322 Lin, C.-C. (2004) Pressure-induced polymorphism in enstatite (MgSiO_3) at room temperature:
323 clinoenstatite and orthoenstatite. *Journal of Physics and Chemistry of Solids*, 65(5), 913-921.
324 <https://doi.org/10.1016/j.jpics.2003.09.028>

- 325 Nestola, F., Ballaran, T.B., Balic-Zunic, T., Secco, L., and Dal Negro, A. (2008) The high-pressure behavior
326 of an Al- and Fe-rich natural orthopyroxene. *American Mineralogist*, 93(4), 644-652.
- 327 Nishi, M., Kubo, T., Ohfuji, H., Kato, T., Nishihara, Y., and Irifune, T. (2013) Slow Si-Al interdiffusion in
328 garnet and stagnation of subducting slabs. *Earth and Planetary Science Letters*, 361, 44-49.
329 <https://doi.org/https://doi.org/10.1016/j.epsl.2012.11.022>
- 330 Okada, T., Narita, T., Nagai, T., and Yamanaka, T. (2008) Comparative Raman spectroscopic study on
331 ilmenite-type $MgSiO_3$ (akimotoite), $MgGeO_3$, and $MgTiO_3$ (geikielite) at high temperatures and
332 high pressures. *American Mineralogist*, 93(1), 39-47.
- 333 Proyer, A., Dachs, E., and McCammon, C. (2004) Pitfalls in geothermobarometry of eclogites: Fe^{3+} and
334 changes in the mineral chemistry of omphacite at ultrahigh pressures. *Contributions to
335 mineralogy and petrology*, 147, 305-318.
- 336 Ringwood, A.E. (1975) *Composition and Petrology of the Earth's Mantle*. 618 p. McGraw-Hill, New York.
- 337 Ringwood, A.E., and Irifune, T. (1988) Nature of the 650 km seismic discontinuity: implications for
338 mantle dynamics and differentiation. *Nature*, 331(6152), 131-136.
339 <https://doi.org/10.1038/331131a0>
- 340 Serghiou, G., Boehler, R., and Chopelas, A. (2000) Reversible coordination changes in crystalline silicates
341 at high pressure and ambient temperature. *Journal of Physics-Condensed Matter*, 12(6), 849-
342 857. <https://doi.org/10.1088/0953-8984/12/6/309>
- 343 Shi, F., Wang, Y., Wen, J., Yu, T., Zhu, L., Huang, T., and Wang, K. (2022) Metamorphism-facilitated
344 faulting in deforming orthopyroxene: Implications for global intermediate-depth seismicity.
345 *Proceedings of the National Academy of Sciences*, 119(11), e2112386119.
- 346 Stachel, T., and Harris, J.W. (2008) The origin of cratonic diamonds-Constraints from mineral inclusions.
347 *Ore Geology Reviews*, 34(1), 5-32.
348 <https://doi.org/https://doi.org/10.1016/j.oregeorev.2007.05.002>
- 349 Stangarone, C., Tribaudino, M., Prencipe, M., and Lottici, P.P. (2016) Raman modes in Pbc₂a enstatite
350 ($Mg_2Si_2O_6$): an assignment by quantum mechanical calculation to interpret experimental results.
351 *Journal of Raman Spectroscopy*, 47(10), 1247-1258.
352 <https://doi.org/https://doi.org/10.1002/jrs.4942>
- 353 -. (2023) Raman modes in Pbc₂a enstatite ($Mg_2Si_2O_6$): an assignment by quantum mechanical
354 investigation and possible implications on the determination of intracrystalline ordering.
355 *JOURNAL OF RAMAN SPECTROSCOPY*, 47(2016), 1247-1258.
- 356 Tollan, P., and Hermann, J. (2019) Arc magmas oxidized by water dissociation and hydrogen
357 incorporation in orthopyroxene. *Nature geoscience*, 12(8), 667-671.
- 358 Van Mierlo, W.L., Langenhorst, F., Frost, D.J., and Rubie, D.C. (2013) Stagnation of subducting slabs in
359 the transition zone due to slow diffusion in majoritic garnet. *Nature Geoscience*, 6(5), 400-403.
360 <https://doi.org/10.1038/ngeo1772>
- 361 White, R., Powell, R., and Holland, T. (2001) Calculation of partial melting equilibria in the system Na_2O -
362 CaO - K_2O - FeO - MgO - Al_2O_3 - SiO_2 - H_2O (NCKFMASH). *Journal of metamorphic Geology*, 19(2),
363 139-153.
- 364 Xu, J., Fan, D., Zhang, D., Guo, X., Zhou, W., and Dera, P.K. (2020) Phase Transition of Enstatite-Ferrosilite
365 Solid Solutions at High Pressure and High Temperature: Constraints on Metastable
366 Orthopyroxene in Cold Subduction. *Geophysical Research Letters*, 47(12).
367 <https://doi.org/10.1029/2020gl087363>
- 368 Xu, J., Fan, D., Zhang, D., Ma, M., Zhou, Y., Tkachev, S.N., Zhou, W., and Dera, P.K. (2022) Phase
369 Transitions of Fe-, Al- and Ca-Bearing Orthopyroxenes at High Pressure and High Temperature:
370 Implications for Metastable Orthopyroxenes in Stagnant Slabs. *Journal of Geophysical Research:*
371 *Solid Earth*, 127(1), e2021JB023133. <https://doi.org/https://doi.org/10.1029/2021JB023133>

- 372 Xu, J., Zhang, D., Fan, D., Zhang, J.S., Hu, Y., Guo, X., Dera, P., and Zhou, W. (2018) Phase Transitions in
373 Orthoenstatite and Subduction Zone Dynamics: Effects of Water and Transition Metal Ions.
374 Journal of Geophysical Research: Solid Earth, 123(4), 2723-2737.
375 <https://doi.org/10.1002/2017jb015169>
- 376 Zedgenizov, D., Kagi, H., Ohtani, E., Tsujimori, T., and Komatsu, K. (2020) Retrograde phases of former
377 bridgmanite inclusions in superdeep diamonds. Lithos, 370, 105659.
- 378 Zhang, D., Jackson, J.M., Chen, B., Sturhahn, W., Zhao, J., Yan, J., and Caracas, R. (2013a) Elasticity and
379 lattice dynamics of enstatite at high pressure. Journal of Geophysical Research: Solid Earth,
380 118(8), 4071-4082. <https://doi.org/10.1002/jgrb.50303>
- 381 Zhang, J.S., Reynard, B., Montagnac, G., Wang, R.C., and Bass, J.D. (2013b) Pressure-induced $Pbca$ - $P2_1/c$
382 phase transition of natural orthoenstatite: Compositional effect and its geophysical implications.
383 American Mineralogist, 98(5-6), 986-992. <https://doi.org/10.2138/am.2013.4345>
- 384 Zhao, Y., Schiferl, D., and Shankland, T.J. (1995) A high P-T single-crystal X-ray diffraction study of
385 thermoelasticity of $MgSiO_3$ orthoenstatite. Physics and Chemistry of Minerals, 22(6), 393-398.
386 <https://doi.org/10.1007/BF00213337>

387
388
389
390
391
392
393
394
395
396
397
398
399
400
401
402
403
404
405
406
407
408
409
410

411 **FIGURE 1.** Typical Raman spectra of orthopyroxene at high pressures and 300 K. (a) En_{100} ; (b)
412 $En_{91}Fs_9$; (c) $En_{86}Fs_{11}$; (d) $En_{74}Fs_{21}$. Blue ticks: Raman modes of α -orthopyroxene; red ticks:
413 Raman modes of β -orthopyroxene; orange ticks: Raman modes of γ -orthopyroxene.

414
415
416
417
418

415 **FIGURE 2.** Raman shifts of orthopyroxene with different Fe content at ambient conditions.
416 Solid circles: this study; open circles: previous experimental results (Chopelas, 1999; Huang et
417 al., 2000). Red lines: fitting results.

419 **FIGURE 3.** Raman shifts of En_{100} at high pressures and 300 K. Blue: α -orthopyroxene; red: β -
420 orthopyroxene; orange: γ -orthopyroxene.

421

422 **FIGURE 4.** Raman shifts of $\text{En}_{91}\text{Fs}_9$ at high pressures and 300 K. Blue: α -orthopyroxene; red: β -
423 orthopyroxene; orange: γ -orthopyroxene; circles and diamonds represent different experimental
424 runs.

425

426 **FIGURE 5.** Raman shifts of $\text{En}_{86}\text{Fs}_{11}$ at high pressures and 300 K. Blue: α -orthopyroxene; red:
427 β -orthopyroxene; orange: γ -orthopyroxene; circles and diamonds represent different
428 experimental runs.

429

430 **FIGURE 6.** Raman shifts of $\text{En}_{74}\text{Fs}_{21}$ at high pressures and 300 K. Blue: α -orthopyroxene; red:
431 β -orthopyroxene; orange: γ -orthopyroxene; circles and diamonds represent different
432 experimental runs.

433

434 **FIGURE 7.** Phase diagram of orthopyroxene at high pressures. Red: this study; green: (Lin,
435 2004); pink: (Zhang et al., 2013b); gray: (Zhang et al., 2013a); yellow: (Dera et al., 2013);
436 purple: (Finkelstein et al., 2015); blue: (Xu et al., 2018); orange: (Xu et al., 2020); black: (Xu et
437 al., 2022); circle: Fe-bearing orthopyroxene; diamond: Fe- and Al-bearing orthopyroxene; solid
438 lines: phase boundary for the Al-free orthopyroxene; dash line: phase boundary for the Al-
439 bearing orthopyroxene. The subscript in Al on the figure shows the Al content in orthopyroxene:
440 $\text{Al}/(\text{Mg}+\text{Fe}+\text{Al})$.

441

442 **FIGURE 8.** Unit cell volume (V_0) and isothermal bulk modulus (K_{T0}) of orthopyroxene at
443 ambient conditions. (a) V_0 for α -orthopyroxene; (b) V_0 for β -orthopyroxene; (c) V_0 for γ -
444 orthopyroxene; (d) K_{T0} for α -orthopyroxene; (e) K_{T0} for β -orthopyroxene; (f) K_{T0} for γ -
445 orthopyroxene; We reanalyzed the pressure-volume data in literature with fixed $K_{T0}' = 8$ for α -
446 orthopyroxene (Dera et al., 2013; Hovis et al., 2021; Hugh - Jones and Angel, 1997; Nestola et
447 al., 2008; Xu et al., 2020; Xu et al., 2022; Xu et al., 2018; Zhang et al., 2013a). For both β - and
448 γ -phase, with fixed $K_{T0}' = 4$, V_0 and K_{T0} are from previous experimental studies (Xu et al., 2020;
449 Xu et al., 2022; Xu et al., 2018).

450

451 **FIGURE 9.** Grüneisen parameter of orthopyroxene at high pressures. (a) ν_1 ; (b) ν_{10} ; (c) ν_{24} ; (d)
452 ν_{32} . Blue: En₁₀₀; red: En₉₁Fs₉; orange: En₈₆Fs₁₁; black: En₇₄Fs₂₁. The data are calculated using the
453 single experimental Raman-active mode in this study together with data summarized in Figure 8,
454 Table S5. Calculated uncertainties are shown as vertical ticks on the bottom left.

455

456

457

458

459

460 **TABLE 1.** Regression constants of En_{100} for Raman modes determined in $\Delta\nu = \nu_0 + aP$ at high
 461 pressures and 300 K.

	ν_i	α -orthopyroxene			β -orthopyroxene			γ -orthopyroxene		
		ν_0	a	R^2	ν_0	a	R^2	ν_0	a	R^2
v1	237.9	239.2	1.34	0.985	241.5	0.95	0.987	253.4	0.35	1.000
v2								301.3	0.54	1.000
v3	279.0	282.1	2.04	0.963	304.1	1.40	0.994	279.9	1.83	1.000
v4	302.4	302.0	2.45	0.984	315.6	1.82	0.997	342.2	0.83	1.000
v5								348.8	1.33	1.000
v6										
v7								398.9	0.62	1.000
v8					364.4	2.42	0.983			
v9										
v10	345.4	348.5	4.99	0.994	376.9	2.60	0.992	397.7	1.79	1.000
v11	385.6	385.1	3.16	0.992						
v12	403.0	405.3	3.43	0.986	433.9	1.20	0.970			
v13	421.1	423.2	2.15	0.977	410.8	2.86	0.932			
v14					439.4	2.07	0.979			
v15	446.2	446.4	2.27	0.999	447.1	2.22	0.997	490.2	0.92	1.000
v16								492.3	1.25	1.000
v17								515.1	1.13	1.000
v18					442.0	3.84	0.987	517.3	1.54	1.000
v19	524.4	523.6	2.69	0.995						
v20	540.3	539.8	1.77	0.954						
v21	551.0	551.3	2.66	0.994						
v22	579.9	579.9								
v23	663.8	664.2	3.34	1.000	663.0	3.10	0.998			
v24	686.5	687.3	3.08	0.999	678.4	2.94	0.997	718.0	1.83	1.000
v25					691.9	3.33	0.998			
v26	753.3	753.3								
v27					825.2	2.43	0.994	856.4	1.46	1.000
v28	853.7	847.6	2.11	0.914	844.5	3.44	0.994	881.3	1.46	1.000
v29	933.8	933.0	2.40	0.831						
v30										
v31					1016.5	3.32	0.995			
v32	1011.8	1013.5	5.22	0.998	1029.3	3.83	0.990	1102.2	0.75	1.000
v33	1033.3	1035.0	4.77	0.998	1041.2	4.14	0.993			

462 ν_i , ν_0 , and $\Delta\nu$ are in cm^{-1} , P in GPa, and the constant, a has the corresponding units. ν_i is the frequency measured at
 463 ambient conditions. R^2 is the correlation coefficient.

464

465 **TABLE 2.** Regression constants of $\text{En}_{91}\text{Fs}_9$ for Raman modes determined in $\Delta\nu = \nu_0 + aP$ at high
 466 pressures and 300 K.

	ν_i	α -orthopyroxene			β -orthopyroxene			γ -orthopyroxene		
		ν_0	a	R^2	ν_0	a	R^2	ν_0	a	R^2
v1	236.9	239.5	1.14	0.961	234.6	1.38	0.980	245.6	0.87	0.702
v2								256.7	1.15	0.884
v3		288.8	1.20	0.894	289.9	0.83	0.302	291.7	0.72	0.600
v4	301.3	302.0	1.67	0.858	303.8	1.38	0.964			
v5					316.6	1.98	0.992	339.2	1.11	0.767
v6										
v7										
v8					384.7	1.43	0.909	389.8	1.23	0.654
v9								428.9	0.38	0.846
v10	341.4	348.2	4.83	0.963	381.4	2.40	0.963	427.6	0.83	0.868
v11	378.9	376.5	4.11	0.984						
v12	400.8	405.8	3.58	0.948	435.2	1.23	0.870	442.7	0.90	0.646
v13	416.9	417.0	2.40	0.985	404.7	3.60	0.962	505.6	0.05	0.005
v14										
v15	442.4	442.7	2.74	0.996	442.5	2.67	0.983	501.6	0.77	0.598
v16										
v17										
v18					441.7	4.05	0.968	541.9	0.59	0.081
v19	525.8	524.3	2.82	0.955	518.2	3.36	0.988	545.6	2.24	0.941
v20	539.0	540.0	1.78	0.944	525.9	3.59	0.980	548.6	2.54	0.982
v21	549.4	549.9	3.17	0.984						
v22										
v23	663.1	664.1	3.28	0.995						
v24	684.5	686.9	2.99	0.978	683.6	2.84	0.981	751.4	0.65	0.613
v25					696.2	3.38	0.993	774.7	0.73	0.565
v26	750.8	751.0	3.59	0.996	732.7	3.58	0.990			
v27					819.7	2.75	0.994	886.4	0.59	0.437
v28	858.1	851.8	2.92	0.964	848.8	3.94	0.990	901.1	2.03	0.759
v29	937.7	930.0	3.41	0.972	941.9	2.52	0.981	976.4	1.15	0.786
v30		938.3	6.34	0.965						
v31										
v32	1011.2	1016.1	3.79	0.981	1020.4	3.64	0.990	1068.1	1.86	0.806
v33	1028.9	1032.7	4.89	0.991	1043.6	4.11	0.988	1087.7	2.35	0.815

467 ν_i , ν_0 , and $\Delta\nu$ are in cm^{-1} , P in GPa, and the constant, a has the corresponding units. ν_i is the frequency measured at
 468 ambient conditions. R^2 is the correlation coefficient.

470

471 **TABLE 3.** Regression constants of $\text{En}_{86}\text{Fs}_{14}$ for Raman modes determined in $\Delta\nu = \nu_0 + aP$ at
 472 high pressures and 300 K.

	ν_i	α -orthopyroxene			β -orthopyroxene			γ -orthopyroxene		
		ν_0	a	R^2	ν_0	a	R^2	ν_0	a	R^2
v1	236.0	240.8	0.90	0.814	237.1	0.93	0.955	251.1	0.33	0.411
v2					292.4	0.14	0.409	301.3	-0.11	0.601
v3		288.4	0.99	0.955	295.7	0.53	0.658	325.1	-0.32	0.638
v4	297.3	297.2	1.51	0.938	288.8	1.90	0.959	328.4	0.25	0.644
v5					315.6	1.63	0.947	339.5	0.80	0.853
v6	321.7	324.0	3.27	0.991						
v7										
v8					370.7	1.85	0.896	394.0	1.04	0.757
v9										
v10	340.8	347.2	4.37	0.985	367.9	2.85	0.918	432.5	0.56	0.664
v11	380.6	379.7	3.25	0.986						
v12	399.6	399.6	4.27	0.952	414.9	1.67	0.964	446.6	0.62	0.688
v13	414.4	411.9	2.41	0.960	427.4	1.61	0.345			
v14										
v15	441.6	441.4	2.44	0.981	449.5	1.81	0.932			
v16										
v17								492.6	1.39	0.835
v18	465.1	464.7	2.80	0.986	450.0	3.34	0.957			
v19	521.8	522.2	2.50	0.986	544.5	0.65	0.208			
v20	538.6	537.4	1.58	0.973	537.5	2.21	0.980			
v21	549.5	548.6	2.50	0.995						
v22		575.6	1.95	0.998						
v23	662.2	663.0	3.16	0.998						
v24	683.8	685.3	2.93	0.996	665.3	3.48	0.961	731.3	1.03	0.723
v25					678.5	3.78	0.902	736.2	1.57	0.870
v26										
v27					834.1	2.16	0.834	864.9	1.31	0.651
v28	857.7	850.2	2.18	0.951	833.5	3.89	0.965	903.4	1.42	0.657
v29	936.0	932.2	3.41	0.979	937.7	2.79	0.804	1055.5	-1.02	0.779
v30	938.2	940.9	4.73	0.986						
v31					1005.5	3.83	0.947	1122.6	-0.28	0.685
v32	1009.8	1011.9	5.15	0.993	1026.4	3.86	0.931	1127.7	0.43	0.892
v33	1029.8	1030.5	4.86	0.997	1041.5	3.98	0.902	1172.0	-0.19	0.732

473 ν_i , ν_0 , and $\Delta\nu$ are in cm^{-1} , P in GPa, and the constant, a has the corresponding units. ν_i is the frequency measured at
 474 ambient conditions. R^2 is the correlation coefficient.

476

477 **TABLE 4.** Regression constants of $\text{En}_{74}\text{Fs}_{21}$ for Raman modes determined in $\Delta\nu = \nu_0 + aP$ at
 478 high pressures and 300 K.

	ν_i	α -orthopyroxene			β -orthopyroxene			γ -orthopyroxene		
		ν_0	a	R^2	ν_0	a	R^2	ν_0	a	R^2
v1	231.6	236.1	1.11	0.940	232.44	1.23	0.963	239.0	0.94	0.937
v2										
v3										
v4	294.7	292.9	1.66	0.930						
v5										
v6	312.3	309.8	4.18	0.966						
v7										
v8					373.58	1.61	0.942	313.0	3.52	0.792
v9										
v10	337.4	346.5	4.02	0.973	363.59	2.76	0.981	307.7	4.45	0.877
v11	371.2	366.5	2.69	0.952						
v12	397.6	401.6	3.18	0.981	430.78	0.95	0.790			
v13					411.58	2.58	0.920			
v14										
v15		436.7	2.66	0.967	447.98	1.77	0.937	507.5	0.02	0.801
v16										
v17										
v18										
v19	517.9	517.8	2.69	0.987	481.42	5.10	0.981			
v20	532.0	531.8	1.97	0.966	484.84	5.30	0.988	630.3	0.20	0.777
v21	543.9	545.2	2.82	0.982						
v22		570.9	3.72	0.988	589.48	2.32	0.943	650.2	0.51	0.417
v23	656.7	658.7	3.16	0.986	655.50	3.15	0.997			
v24	678.8	682.1	3.01	0.989	684.93	2.46	0.929	770.7	-0.16	0.827
v25					698.81	2.81	0.951	804.4	-0.45	0.719
v26	748.5	749.2	3.05	0.991						
v27					830.74	2.54	0.970	849.8	2.03	0.691
v28	850.7	848.9	2.97	0.963	819.66	4.77	0.980			
v29	936.3	937.3	2.98	0.940	945.05	2.73	0.944			
v30		952.2	3.61	0.994						
v31										
v32	1002.6	1007.6	5.02	0.995	1005.46	3.65	0.964	1095.3	0.76	0.670
v33	1020.1	1028.4	4.16	0.974	1021.91	4.29	0.962	1119.7	1.06	0.662

479 ν_i , ν_0 , and $\Delta\nu$ are in cm^{-1} , P in GPa, and the constant, a has the corresponding units. ν_i is the frequency measured at
 480 ambient conditions. R^2 is the correlation coefficient.
 481

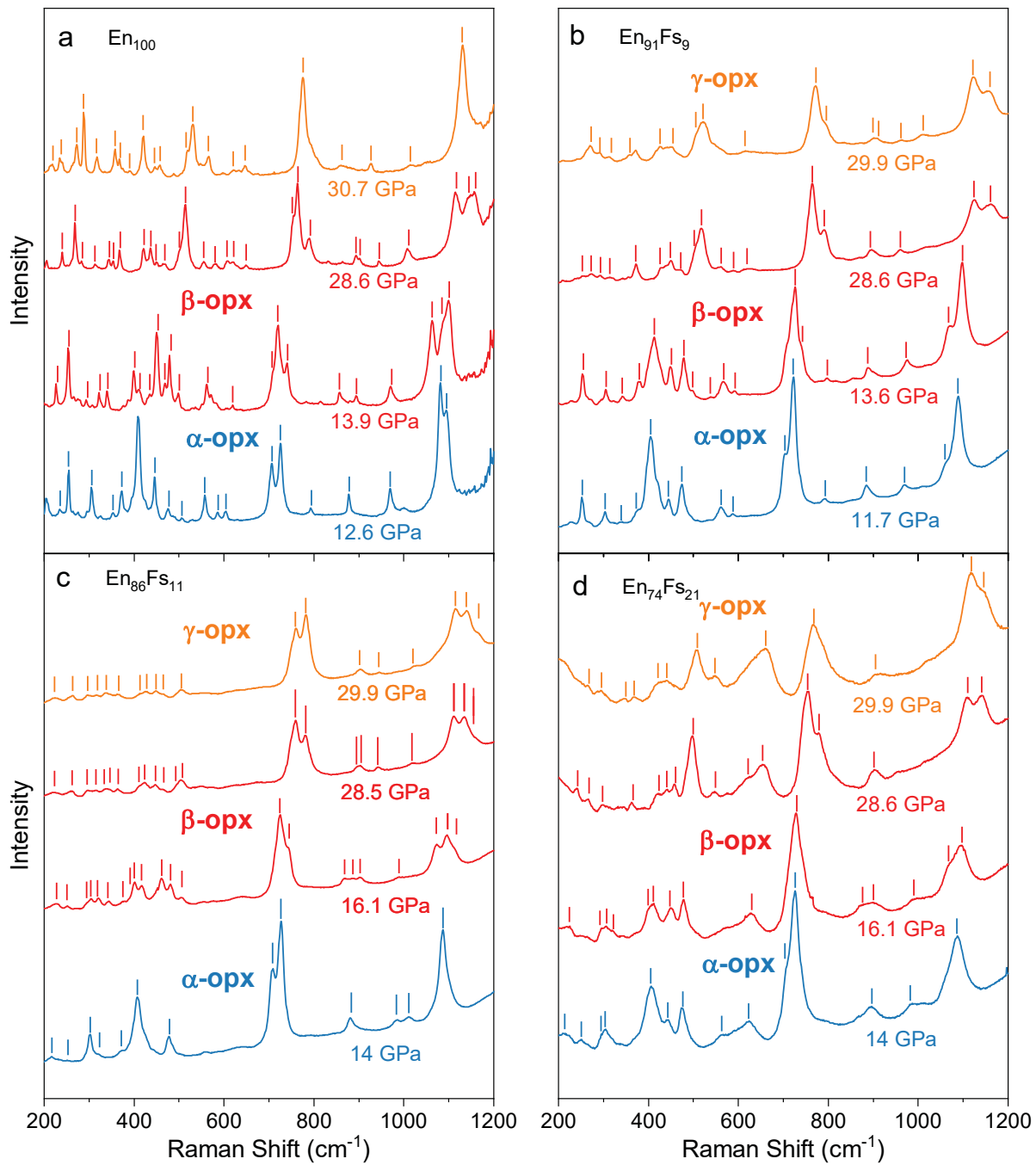


Fig 1

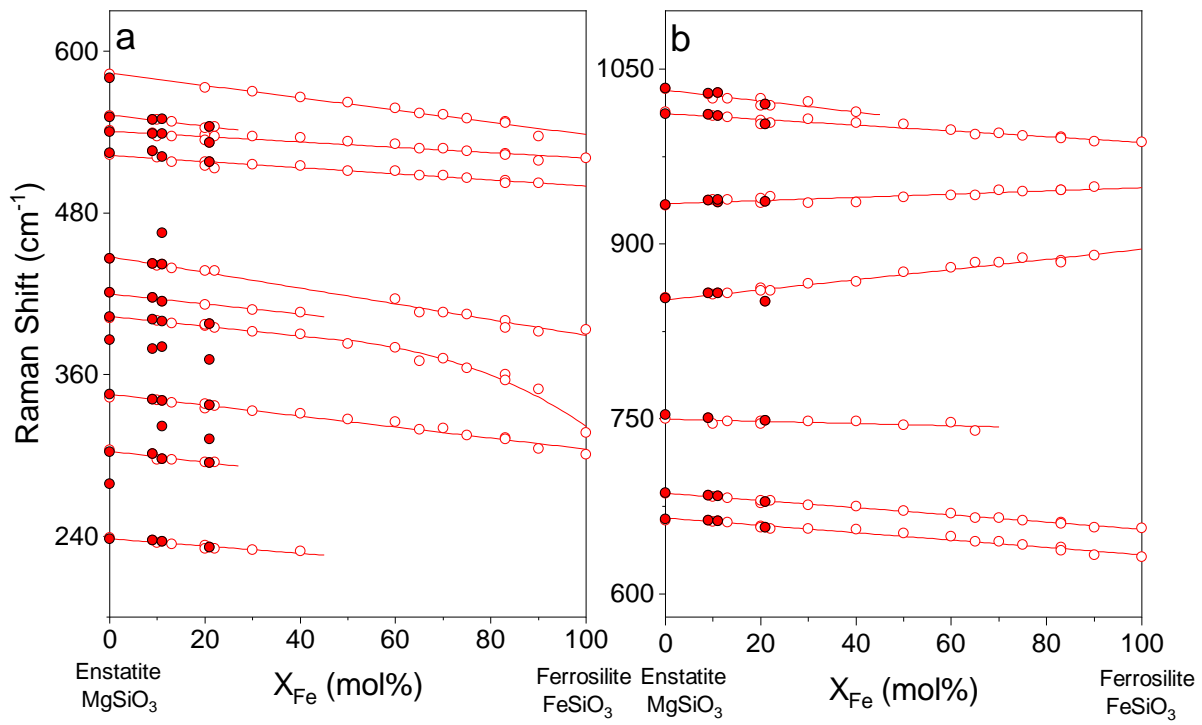


Fig 2

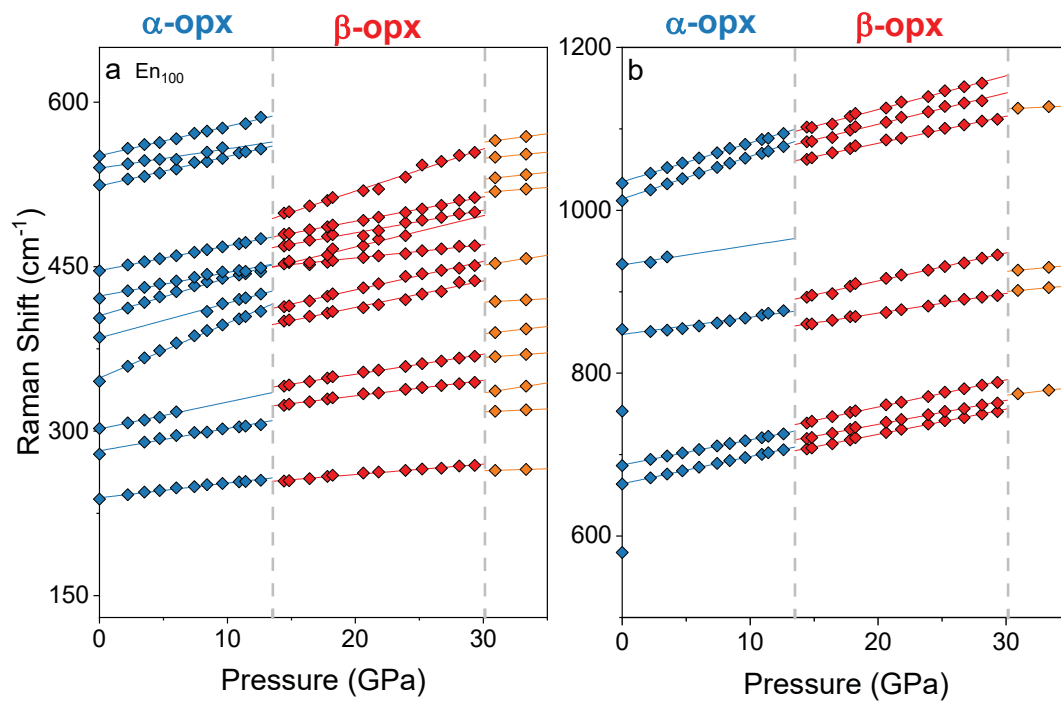


Fig 3

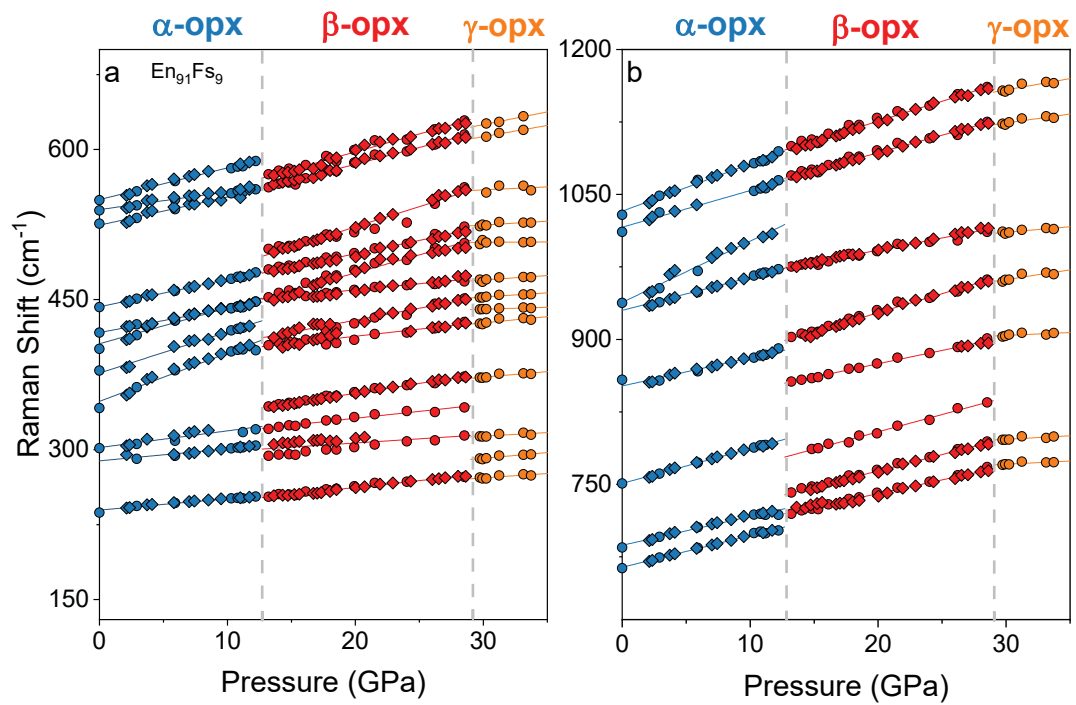


Fig 4

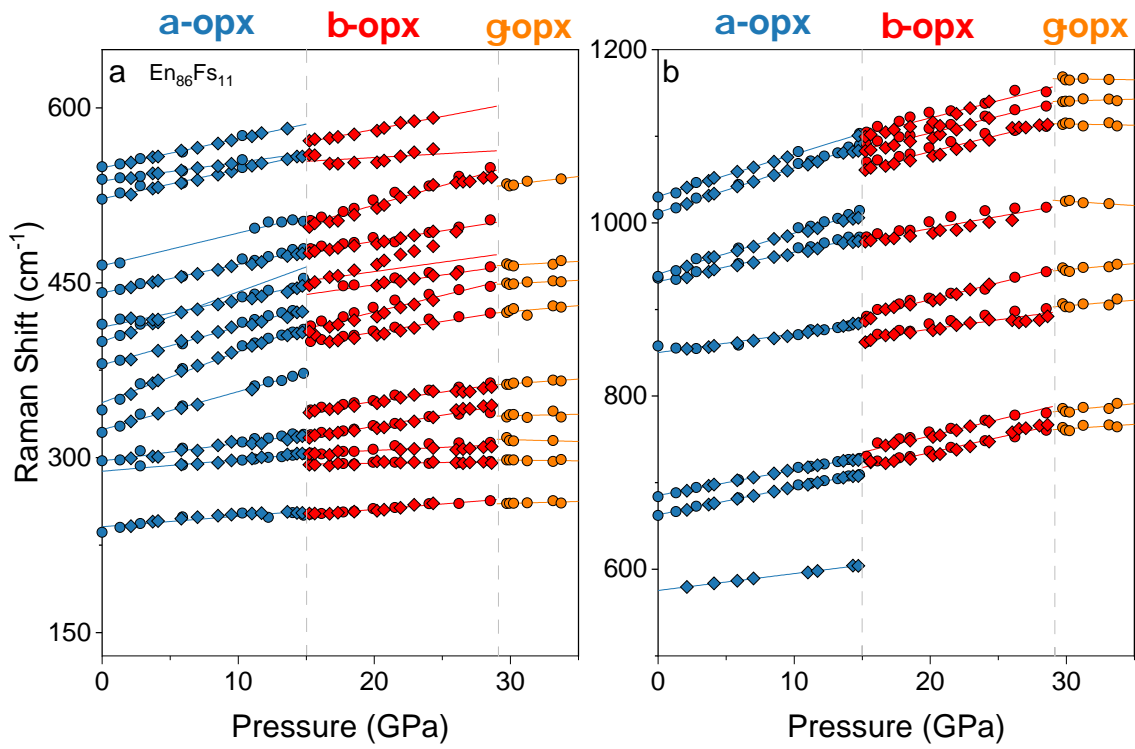


Fig 5

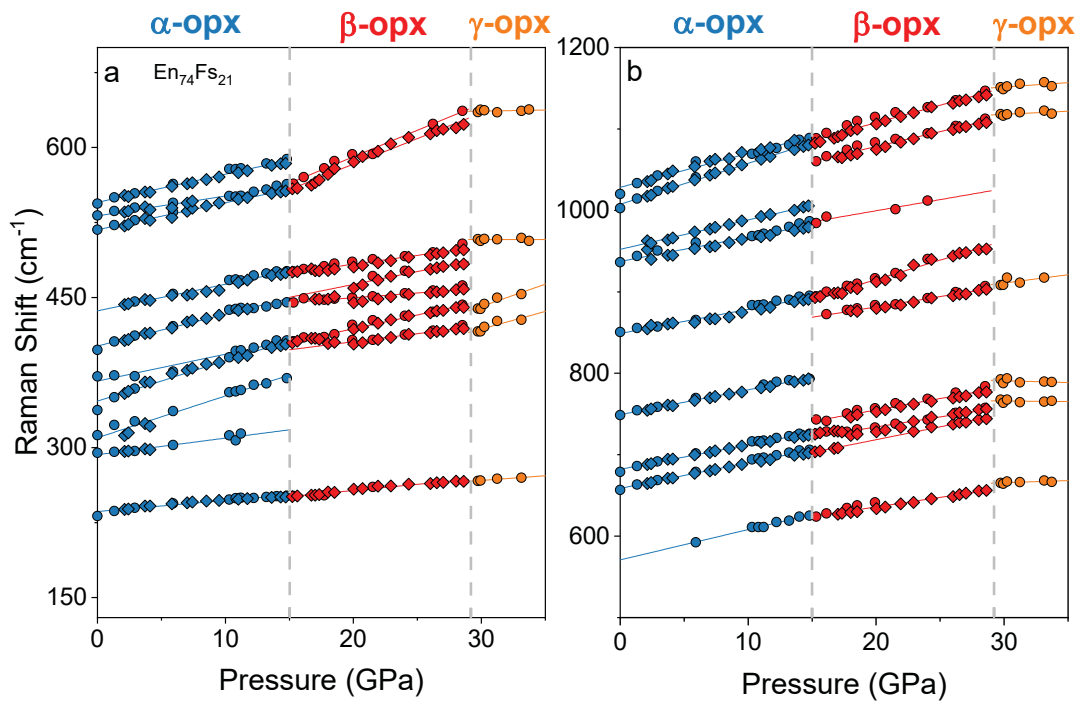


Fig 6

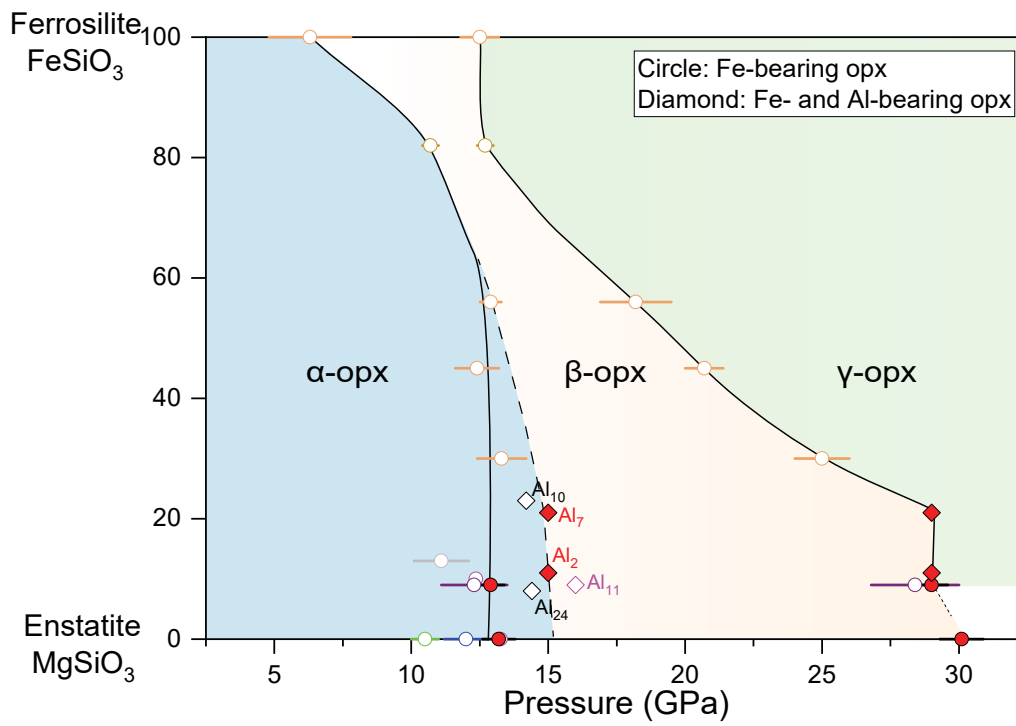


Fig 7

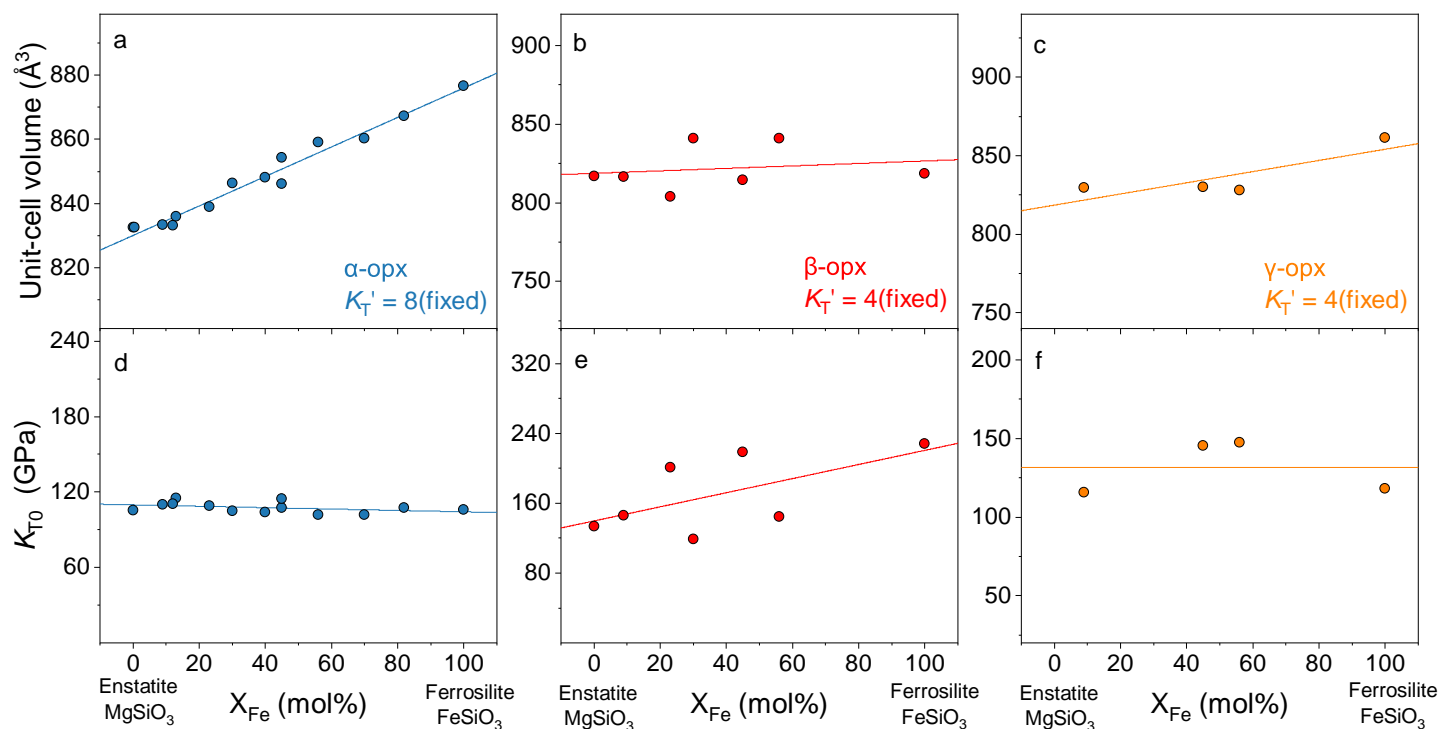


Fig 8

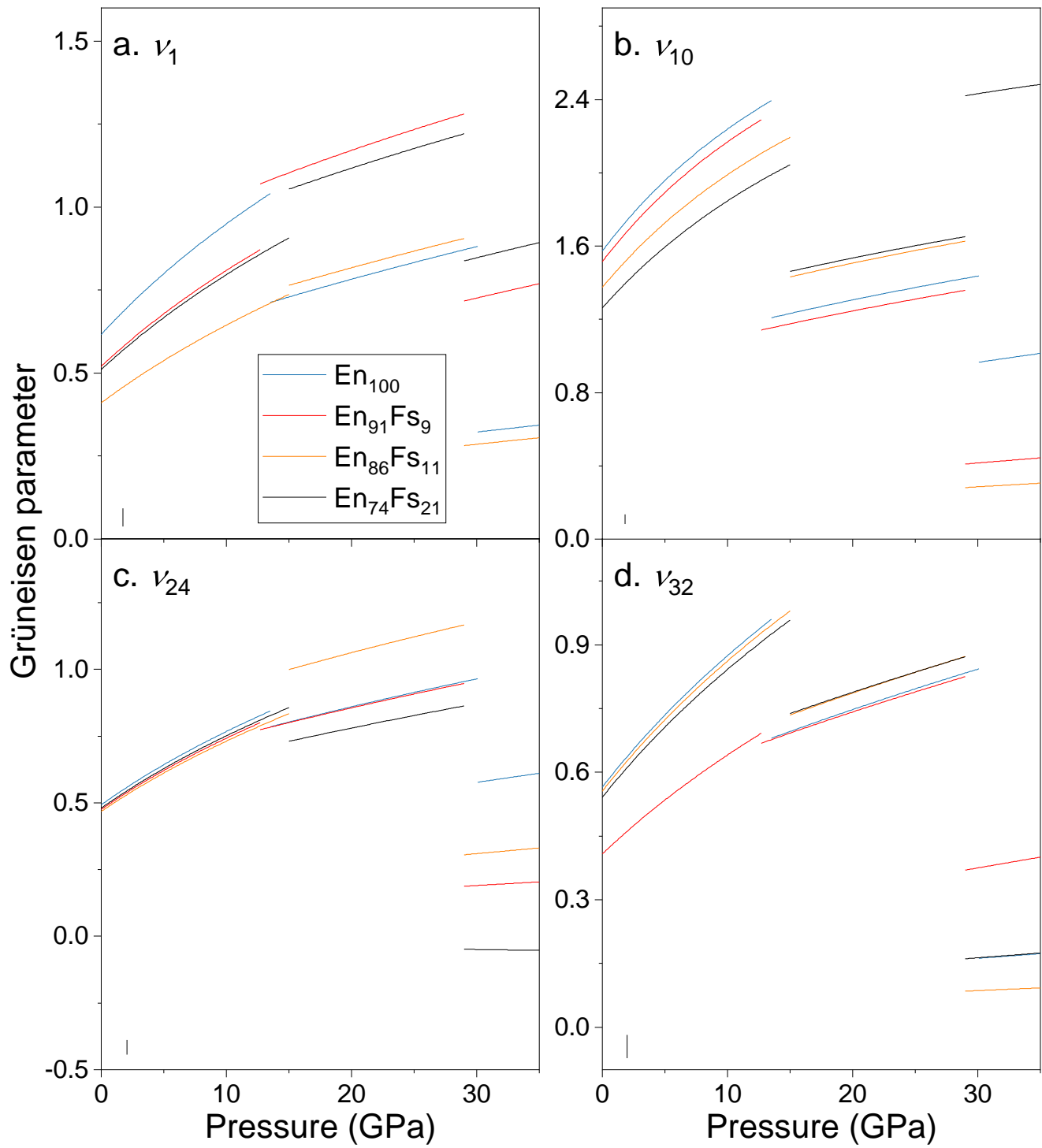


Fig 9